International Journal for Multiscale Computational Engineering, 15(2): 99–119 (2017)

CONCURRENT ATOMISTIC-CONTINUUM MODEL FOR DEVELOPING SELF-CONSISTENT ELASTIC CONSTITUTIVE MODELING OF CRYSTALLINE SOLIDS WITH CRACKS

Jiaxi Zhang, Subhendu Chakraborty, & Somnath Ghosh*

Department of Civil Engineering, Johns Hopkins University, Baltimore, Maryland 21218, USA

*Address all correspondence to: Somnath Ghosh, Michael G. Callas Professor, Johns Hopkins University, E-mail: sghosh20@jhu.edu

Original Manuscript Submitted: 3/7/2017; Final Draft Received: 3/12/2017

Damage of materials inherently involves coupling of deformation and failure mechanisms at multiple length and time scales. This paper develops self-consistent elastic constitutive relations of crystalline materials containing atomistic scale cracks, from observations made in a concurrent multi-scale simulation system coupling atomistic and continuum domain models. The self-consistent constitutive model incorporates both nonlinearity and nonlocality to account for atomic level interactions and deformation mechanisms, especially near crack tips. Atomistic modeling in the concurrent model is done using molecular dynamics (MD), while the continuum modeling is done using a crystal elasticity finite element (FE) analysis code. The atomistic–continuum coupling is achieved by enforcing geometric compatibility and force equilibrium in an interface region. The constitutive model is calibrated by comparing with the results of MD predictions in the concurrent model. For validation, the crack tip stress field is investigated using both the coupled concurrent model and a FE model with the constitutive law. The self-consistent model exhibits excellent accuracy and enhanced efficiency in comparison with pure MD and concurrent model results.

KEY WORDS: *self-consistent elastic model, concurrent atomistic-continuum coupling, crack tip field, molecular dynamics, finite element analysis*

1. INTRODUCTION

Damage of metals and alloys inherently involves coupling of various deformation and failure mechanisms at multiple length and time scales. They include atomic-scale bond-breaking, sub-micrometer-scale defects and dislocation activities, micrometer-scale intra- and transgranular cracks in grains and grain boundaries, and macro-scale fracture zones in structural components. While computational modeling of deformation in polycrystalline materials is making major strides in predicting stress–strain behavior with reasonable accuracy, failure, fatigue, and ductility predictions are still far from mature. A significant bottleneck with simulations leading to failure prediction is because the crack growth phenomenon in crystalline alloys is not adequately understood or characterized. A majority of simulations that attempt to model cracking in polycrystalline materials incorporate cohesive zone models (CZM) with experimentally fitted parameters. Cohesive zone models (Ortiz and Pandolfi, 1999; Roe and Siegmund, 2003) interpret fracture as a gradual process, where the separation between material surfaces is resisted by cohesive tractions. Numerical models in Columbus and Grujicic (2001) and Grujicic et al. (2003) have used the CZM alongside crystal plasticity models to simulate crack opening and tip behavior. Their CZM potentials have been determined through the use of molecular statics simulations of the interface decohesion. While CZM models enjoy the ease of numerical implementation, these laws in some cases lack appropriate representation of deformation and other mechanisms near the crack tip that govern crack growth. There is a need to create a framework for coupling continuum scale deformation with atomic-scale crack evolution in a suitable description that can be used in continuum modeling of crack growth.

1543–1649/17/$35.00

Atomistic simulations using molecular dynamics (MD) has been widely used to simulate crack growth, e.g., in Abraham et al. (1997); Farrissey et al. (2000); Gumbsch (1995); Shimomura et al. (2003); Yamakov et al. (2006); Zhang and Ghosh (2013); Zhou et al. (1998); Zhu et al. (2004). These studies have provided insights on deformation mechanisms associated with crack propagation. A 320 billion atom simulation, using the Lennard-Jones (L-J) two-body potential has been realized on the BlueGene/L in Kadau et al. (2006) reaching the micrometer length scales. A 35 million atom system has been studied in Zhou et al. (1998) for ductile fracture in copper using the EAM potential that exhibits the emission of dislocation loops from the crack tip. Despite advances in parallel computing, MD simulation of crack propagation in systems corresponding to continuum length and time scales still remains a challenge. This prompts the need for continuum models of crack evolution conforming to observations from atomistic simulations. One of the earliest attempts to develop a cohesive model using MD for interface separation was in Spearot et al. (2004) for a copper bi-crystal with interface under normal and shear loading. Cohesive zone relations have been extracted for brittle cracks from atomic interaction potential in Zhou et al. (2008), whereas simple virial stress–strain relations have been used to obtain traction–displacement relationships for aluminum bi-crystal interfaces in Yamakov et al. (2006, 2008).

Tracking individual atoms in the atomistic systems puts severe constraints on both spatial and temporal scales in MD simulations. This is compounded by non-physical boundary conditions, e.g., periodic boundary conditions for atomic representative volumes containing cracks. Hierarchical upscaling is a common approach to conduct larger scale simulations, where homogenized constitutive relations may be derived from MD simulations. Concurrent, coupled atomistic–continuum models combine the lower scale (MD) and higher scale (continuum) description in a single framework, and let the two systems evolve simultaneously with force balancing and compatibility conditions enforced at the interface. This physically represents spatially larger systems and hence helps overcoming the limitations of pure atomistic simulations. Various concurrent multi-scale models coupling atomistic and continuum systems have been developed by research groups. They include the finite element-atomistic (FEAt) (Kohlhoff et al., 1991), quasi-continuum (QC) (Miller et al., 1998; Tadmor, 1996), bridging scale methods (BSM) (Wagner and Liu, 2003), bridging domain (BD) (Xiao and Belytschko, 2004), coupled atomistic and discrete dislocation (CADD) (Warner et al., 2007), atomistic-to-continuum (ATC) (Badia et al., 2007, 2008), embedded statistical coupling method (ESCM) (Saether et al., 2009), coarse-grained atomistic models (CAC) (Xiong et al., 2012) and multi-resolution molecular mechanics (MMM) by Yang and To (2015). Fish et al. (2007) and Fish and Chen (2004) have developed concurrent atomistic to continuum coupling approaches based on multigrid principles for solving large molecular statics and molecular dynamics systems. Their work incorporates fine-scale features in atomistic domains with continuum model for macroscale deformation along with an interphase sub-domain. The common goal of these concurrent models is to yield results similar to the full atomistic simulations with significantly less computational cost. These models have several concerns stemming from error in the interphase region, ghost force correction, implementation of finite temperature conditions, etc. In Miller and Tadmor (2009), the authors have carefully reviewed various coupling methods and compared the computational efficiency and accuracy. For metals, coupled atomistic–continuum models have been used to study grain boundary dislocation activity in Dewald and Curtin (2007), competing dislocation nucleation and crack propagation in Yamakov et al. (2014), nano-indentation in Picu (2000), traction–displacement relationships at crack tip in Xu et al. (2016); Yamakov et al. (2008). While substantial progress has been made with respect to understanding the crack tip processes by these concurrent models, certain challenges still remain. Most coupled models only deal with zero-temperature systems, while finite temperature systems under constant strain-rate loading are essential to capture the temperature and strain-rate effects for critical events. Another is the effect of non-linearity and non-locality on crack tip stress field that is not well characterized. Both issues are important for obtaining accurate crack evolution and associated deformation mechanisms using the concurrent atomistic–continuum model.

The goal of this paper is to develop a concurrent multi-scale simulation system, coupling atomistic and continuum domain models with the intent of using it to generate a self-consistent, physics-based elastic constitutive relation for a cracked crystalline material. The coupled concurrent model has a finite-temperature feature and is suitable for constant strain-rate loading. Numerical issues such as ghost-forces, phonon reflection, and consistency between atomic interaction and continuum constitutive relation are carefully treated to minimize error in the interface between the disparate domains. The finite-temperature concurrent multi-scale system embeds an atomistic domain with a crack in an elastic continuum domain for crystalline solids, for which self-consistent constitutive relations are

determined. Atomistic simulations are conducted by molecular dynamics or MD, while the continuum scale analyses are conducted by the finite element (FE) method. The interface handshake domain is intended to satisfy conditions of geometric compatibility and force equilibrium between the two disparate domains. A *self-consistent homogenization* process is conducted to hierarchically derive a nonlinear, nonlocal elastic constitutive model from the concurrent model simulations. Parameters in the self-consistent constitutive model are calibrated from results of simulations with the coupled concurrent system. This constitutive model is validated by comparing crack tip fields obtained by FE simulations of the continuum domain with those in the atomistic domain of the concurrent model.

The overall focus of the model is on systems subjected to quasi-static loading, i.e., systems with negligible inertia effect. For continuum systems this implies that inertia is neglected when analyzing deformation and stresses under incremental loading. For the atomistic system however, finite-temperature MD simulations are needed to capture thermally activated crack tip processes like crack propagation and dislocation emission in crystalline materials which are temperature- and strain-rate-dependent. To establish compatibility and traction reciprocity with quasi-static continuum simulations, equilibrated atomistic configurations corresponding to time-averaged trajectories of atomic fluctuation are implemented in the concurrent model. This procedure overcomes the need to implement a fully dynamic coupled model, which poses difficulties in time scaling and may yield spurious interfacial modes. For example, the minimum wavelength for stability conditions in a continuum FE mesh can give rise to spurious effects like wave reflection with artificial heating in the handshake region, as well as other forms of numerical instability (Junge et al., 2015).

The paper starts with a formulation of the concurrent model for coupling atomistic–continuum simulations in Section 2. Section 3 discusses the numerical implementation steps and algorithms, including efficient solution with sub-stepping, ghost force correction, temperature control, and phonon absorption. A self-consistent constitutive model is developed using the coupled concurrent model in Section 4. This model is used to study crack propagation and dislocation activity in single-crystal nickel in Section 5. The paper ends with a summary in Section 6.

2. A CONCURRENT FRAMEWORK FOR COUPLED ATOMISTIC–CONTINUUM SIMULATIONS

A concurrent simulation framework, coupling molecular dynamics (MD) and finite element (FE) continuum elasticity models for crystalline solids under quasi-static loading, is developed in this section. MD simulations are carried out efficiently by the parallel Large-scale Atomic/Molecular Massively Parallel Simulator or *LAMMPS* (Plimpton, 1995), while the FE simulations are conducted by codes developed in the Ghosh group.

2.1 Domain Partitioning and System Setup

As shown in Fig. 1, the computational domain is divided into three sub-domains of concurrent simulations. These include the atomistic domain Ω_A of MD simulations, the continuum domain Ω_C of FE simulations, and an interfacial handshake domain Ω_I of compatibility constraints between MD and FE simulations. The FEM model for the continuum domain Ω_C assumes quasi-static conditions with inertia effects neglected. The constitutive model in Ω_C is developed from self-consistent homogenization with the atomistic model.

Two types of models have been proposed for coupling atomistic and continuum simulations. These are the energy-based and force-based coupled models. The energy forms for pure atomistic and continuum regions are well defined, and the difference emanates from the interface region treatment in the coupled models. The energy-based formulation admits an additive decomposition of total energy functional for the coupled system (for static problems) or the Hamiltonian (for dynamic problems) into respective energy functionals for each subdomain. Minimization of these energy functionals correspond to the static or dynamic equilibrium conditions. While the energy approach provides a mathematically clean description, a difficulty is with finding the appropriate energy functional that eliminates ghost forces arising from the non-local atomic interactions. The force-based formulation has to deal with a local problem of constructing constraint forces on each degree of freedom, and solving the force equilibrium problem (Newton's equations). This approach generally results in a better control over spurious ghost forces, and yields more accurate forces in the interfacial domain. However, since the latter formulation does not define an energy functional, convergence toward an equilibrium configuration can be slow. Special attention is required to guarantee that the equilibrium

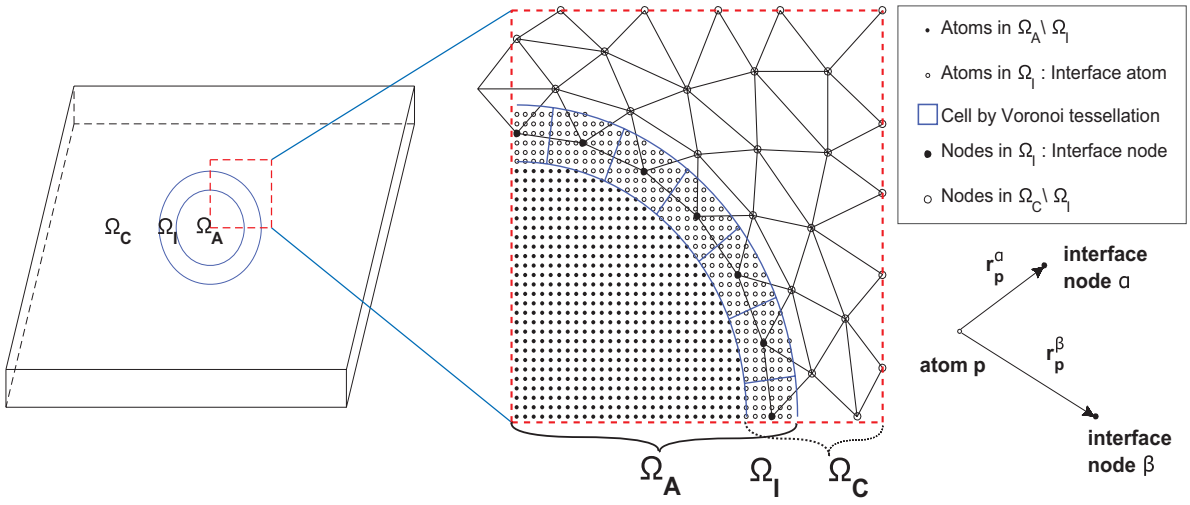

FIG. 1: Schematic of the partitioned computational domain, showing models for the MD, continuum, and interface regions

solution is stable. The present work implements a force-based coupling method for a better representation of the ghost forces and geometric compatibility.

The interface handshake region $\Omega_I = \Omega_A \bigcap \Omega_C$, where both the continuum and atomistic models overlap, couples the sub-domains Ω_A and Ω_C. Following coupling methods in Saether et al. (2009), Ω_I comprises a layer of finite elements with nodes characterized as interface nodes, and a band of underlying interface atoms. Each interface node in the FE model is associated with a cluster of interface atoms, assigned using a 3D Voronoi tessellation method (Ghosh, 2011). In this process, the Voronoi cell associated with an interface node i contains all interface atoms α, for which the distance $r_p^\alpha \leq r_p^\beta \;\; \forall\, \alpha \neq \beta$, where r_p^α is the distance between the node α and atom p. Compatibility conditions are enforced between each interface node in the FE model and the cluster of interfacial atoms. In this approach, spatially averaged displacements of interface atoms are equated to the displacement fields of the interface node to implement the atom-node compatibility condition in a weak sense. This results in a weak satisfaction of the force equilibrium condition between the atomistic and continuum models, as discussed in Section 2.2. A single layer of FE nodes in the interfacial region is considered in this paper to facilitate surface coupling. Alternate strategies of volumetric coupling have been pursued for the interface region with gradual blending of either force or energy fields in Xiao and Belytschko (2004) and Badia et al. (2007). The equilibrium solutions of the surface and volumetric approaches have been compared in Davydov et al. (2014) for a uniform plate and a plate with center hole. Results infer that while similar accuracy is obtained in comparison with analytical solutions, the surface coupling is easier to implement and computationally more efficient.

2.2 Governing Equations

An incremental formulation is adopted to account for the solution of the quasi-static continuum problem involving non-linear material constitutive relations. In the following, indices α, β will be used to denote finite element nodes, indices p, q to identify atoms, and index i for the coordinate axes. The incremental energy functional, corresponding to a load increment from the previous equilibrated configuration, is given as the sum of contributions from the atomistic, continuum, and interface regions as

$$\Delta\Pi_{tot} = \Delta\Pi_C + \Delta\Pi_A + \Delta\Pi_I \tag{1}$$

where the right-hand side (RHS) corresponds to contributions from respective domains. Since inertia is neglected for the continuum FE analysis and the atomic motion due to thermal fluctuation is time-averaged in the coupling, the kinetic energy contribution to the overall Lagrangian is neglected. Correspondingly, the equilibrium state for the quasi-static problem is obtained by minimizing the total potential energy functional in Eq. (1). The contributions from

the continuum domain Ω_C is given as:

$$\Delta\Pi_C = \int_{\Omega_C} \boldsymbol{\sigma} : \Delta\boldsymbol{\epsilon} dV - \int_{\partial\Omega_C} \boldsymbol{t} \cdot \Delta\boldsymbol{u}^C dA = \{\boldsymbol{f}_{\text{C-int}} - \boldsymbol{f}_{\text{C-ext}}\} \cdot \{\Delta\boldsymbol{u}^C\} \tag{2}$$

The first term on the RHS corresponds to the incremental strain energy of the continuum in Ω_C, with $\boldsymbol{\sigma}$ and $\Delta\boldsymbol{\epsilon}$ corresponding to the Cauchy stress and incremental infinitesimal strain tensors, respectively. The load vector $\boldsymbol{t}$ in the work potential denotes the traction applied on the boundary of the domain $\partial\Omega_C$. The internal force vector $\{\boldsymbol{f}_{\text{C-int}}\} = \bigcup_{\alpha\in\Omega_C}\{\boldsymbol{f}^{\alpha}_{\text{C-int}}\}$ is the union of force vectors at every node α of the FE mesh in $\partial\Omega_C$. It is evaluated by taking the derivative of the discretized form of the FE strain energy with respect to nodal degrees of freedom $\Delta\boldsymbol{u}^C$. The external force vector $\{\boldsymbol{f}_{\text{C-ext}}\}$ on all boundary nodes of the FE mesh is computed from the applied traction on the FE boundary $\partial\Omega_C$.

The contributions from the atomistic domain Ω_A is

$$\Delta\Pi_A = \sum_{p\in\Omega_A} \Delta\Phi_p(\bar{\boldsymbol{r}}) - \sum_{p\in\Omega_A} \boldsymbol{f}^p_{\text{A-ext}} \cdot \Delta\bar{\boldsymbol{r}}_p \tag{3}$$

where $\Delta\Phi_p(\bar{\boldsymbol{r}})$ is the incremental energy of an atom p given by inter-atomic potential as function of position vector of all atoms $\bar{\boldsymbol{r}}$. An example is the multi-body potential function described by the embedded-atom method or EAM (Mishin et al., 1999), which is appropriate for most transition metal systems. The term $\boldsymbol{f}^p_{\text{A-ext}}$ denotes the external forces applied on the atom p from external sources and $\Delta\bar{\boldsymbol{r}}_p$ is the position vector increment of the atom p, and the summation is over all atoms in Ω_A. The relation between the displacement vector $\boldsymbol{r}_p$ of atom p and its time-averaged value $\bar{\boldsymbol{r}}_p$ is given as:

$$\bar{\boldsymbol{r}}_p(t) = \frac{1}{N}\sum_{j=0}^{N-1} \boldsymbol{r}_p(t - j\cdot\Delta t^{md}) \tag{4}$$

where t is the time, $\boldsymbol{r}_p(\tau)$ is the position vector of an atom p at time τ, Δt^{md} is the uniform time step taken in the N sampling time-integration steps for MD simulations. $N\Delta t^{md}$ should be chosen larger than the period T of thermal vibration of the atomistic system such that the average does reflect the displacement due to mechanical loading. In this paper, T is set to be 1 ps with $N = 500$ and $\Delta t^{md} = 2$ fs.

Finally the contribution from interfacial handshake domain Ω_I is obtained from the constraint compatibility condition using Lagrange multipliers, as

$$\Delta\Pi_I = \sum_{\beta\in\Omega_I} \boldsymbol{\lambda}_\beta \cdot \boldsymbol{C}_\beta \tag{5}$$

where $\boldsymbol{\lambda}_\beta = \{\lambda^1_\beta, \lambda^2_\beta, \lambda^3_\beta\}$ is the array of Lagrange multipliers for the constraint function $\boldsymbol{C}_\beta = \{C^1_\beta, C^2_\beta, C^3_\beta\}$ at an interface node β. The constraint function $\boldsymbol{C}_\beta$ describes the geometry compatibility of a interface node β in Ω_I, where the average displacement of atoms inside the Voronoi cell G_β equals the displacement of that node. For an incremental displacement, the relation is given as

$$C_\beta(\Delta\boldsymbol{u}^C, \Delta\boldsymbol{u}^A) = \Delta\boldsymbol{u}^C_\beta - \sum_{p\in G_\beta} w_p \cdot \Delta\boldsymbol{u}^A_p = 0 \quad \forall\beta \in \Omega_I \tag{6}$$

where $\boldsymbol{u}_p = \boldsymbol{r}_p - \boldsymbol{r}^0_p$ is the displacement vector of atom p, w_p is a weighting function for atom $p \in G_\beta$ with $\sum_{p\in G_\beta} w_p = 1$, and $\boldsymbol{u}_\beta$ is the displacement vector of interface node β. The superscripts C and A will be dropped in the subsequent discussions as their association with the node number β or the atom number p automatically designate their domain. For coupling finite-temperature atomistic simulations with quasi-static continuum simulations, a time-averaged displacement vector $\bar{\boldsymbol{u}}_p$, corresponding to the atomic position vector defined in Eq. (4), is used. The corresponding compatibility condition is expressed as

$$\Delta\boldsymbol{u}_\beta(t) = \sum_{p\in G_\beta} w_p \cdot \Delta\bar{\boldsymbol{u}}_p(t) = \sum_{p\in G_\beta} w_p \cdot \frac{1}{N}\left[\sum_{j=0}^{N-1} \Delta\boldsymbol{u}_p(t - j\cdot\Delta t^{md})\right] \tag{7}$$

The equilibrium condition of the coupled system is realized by setting the first variation of the energy functional Eq. (1) to zero, i.e., $\delta(\Delta\Pi_{tot}) = 0$. Substituting Eqs. (2), (3), (5), and (6) in Eq. (1), this condition is derived for nodal points in the continuum FE domain and atoms in the MD domain for directions $i = 1, 2, 3$ as

$$\frac{\partial \Delta\Pi_{tot}}{\partial \Delta u^i_\alpha} = f^i_\alpha = \begin{cases} (f^i_\alpha)_{\text{int}} - (f^i_\alpha)_{\text{ext}} + \lambda^i_\alpha & \text{for node} \quad \alpha \in \Omega_I \\ (f^i_\alpha)_{\text{int}} - (f^i_\alpha)_{\text{ext}} & \text{for node} \quad \alpha \in \Omega_C \backslash \Omega_I \end{cases} = 0 \tag{8a}$$

$$\frac{\partial \Delta\Pi_{tot}}{\partial \Delta \bar{r}^i_p} = f^i_p = \begin{cases} (\partial\Delta\Phi(\boldsymbol{r}))/(\partial\Delta\bar{u}^i_p) - (f^i_p)_{\text{ext}} - w_p\lambda^i_\alpha & \text{for atom} \quad p \in G_\alpha \quad \text{in} \quad \Omega_I \\ (\partial\Delta\Phi(\boldsymbol{r}))/(\partial\Delta\bar{u}^i_p) - (f^i_p)_{\text{ext}} & \text{for atom} \quad p \in \Omega_A \backslash \Omega_I \end{cases} = 0 \tag{8b}$$

where G_α is the Voronoi cell domain associated with finite element node α. In Eq. (8a) the total conjugate force component f^i_α at a node α is from contributions due to strain energy $(f^i_\alpha)_{\text{int}}$, external forces $(f^i_\alpha)_{\text{ext}}$, and Lagrange multipliers λ^i_α representing reaction force on node α from atomistic system due to compatibility constraint. For the atomistic domain, f^i_p is the time-averaged total conjugate force component on an atom p in its time-averaged position $\bar{r}^i_p$. It comprises the inter-atomic force component $(\partial\Delta\Phi(\boldsymbol{r}))/(\partial\Delta\bar{u}^i_p)$, external forces $(f^i_p)_{\text{ext}}$, and the constraint force contribution to individual atoms $w_p\lambda^i_\alpha$, where w_p is a weighting function, such that

$$(\lambda^i_\alpha)^C + \left(\sum_{p \in G_\beta} w_p \lambda^i_\alpha \right)^A = 0 \tag{9}$$

The compatibility constraint between atomistic and continuum models in the handshake region, represented by Eqs. (6) and (9), is satisfied in a weak sense by spatial averaging in this model. Hence, it will have local errors in the displacement and stress fields for atoms in Ω_I. The error is however expected to decay significantly with increasing distances from the interface region into Ω_C or Ω_A, where deformation mechanisms are operative.

The MD equations in the domain Ω_A needed for solving the coupled Eqs. (8) yielding thermal fluctuations of atoms are given by

$$m_p \ddot{\boldsymbol{u}}_p = \boldsymbol{f}_p \tag{10}$$

where m_p is the mass of an atom p with an applied force $\boldsymbol{f}_p$. To maintain the temperature of the system and absorb elastic waves, temperature control is applied through Langevin dynamics on the atoms in the interface region Ω_I. The NVE ensemble is used for the pure atomistic domain Ω_A, with additional random force plus damping applied. Thus the forces on the interior atoms remain unchanged, while the forces on interface atoms are given as

$$\boldsymbol{f}_p = \boldsymbol{f}^0_p - \gamma m_p \dot{\boldsymbol{r}}_p + \sqrt{2\gamma(\vec{r}) k_B \theta m_p}\, R(t) \;\; \forall p \in \Omega_I \tag{11}$$

where m_p is the mass, $\boldsymbol{f}^0_p = -\boldsymbol{\nabla}_p \Phi + w_p \boldsymbol{\lambda}_\beta + \boldsymbol{f}^p_{\text{A-ext}}$ is the initial force as given by Eq. (8b), k_B is the Boltzmann constant, θ is the target temperature, $\gamma(\vec{r})$ is the damping coefficient as function of atomic position, and $R(t)$ is a delta-correlated stationary Gaussian process with zero-mean value. The damping strategy is "stadium" damping or "ramped" damping introduced first in Holian et al. (1995) and also discussed in Qu et al. (2005), where the damping coefficient gradually increase from 0 to a certain value γ_0 in the interface region. The damping term in Eq. (11) helps suppress the elastic wave propagation in the interface region. This is important for numerical stability of the dynamic coupled model, according to studies in Pavia and Curtin (2015).

3. NUMERICAL IMPLEMENTATION OF THE COUPLED CONCURRENT MODEL

The coupled system of continuum-atomistic Eqs. (8), corresponding to quasi-static equilibrated states with varying loads, are solved in an incremental manner using a successive iterative approach with interfacial load balancing. Rather than simultaneous solutions of a fully coupled system, a staggered-iterative solution approach is pursued in this work. The method solves respective problems for each of the domains Ω_C and Ω_A in each iteration subject to

the constraint forces and displacements, passed through the interface domain Ω_I. This enables the implementation of appropriate algorithms and solvers for each domain.

MD simulations are carried out by the *LAMMPS* code (Plimpton, 1995), and FE simulations are conducted crystal elasticity codes developed in the authors' group. Appropriate interface modules and data structure are used in the integration of these codes. The Message Passing Interface (MPI) is used for distributing processors to perform MD and FE simulations. Prior to passing information between FE and MD computations, the parallel distributed data for global vectors are gathered and processed. This requires allocation of additional memory since either FE processors store atomistic data and/or MD processors store FE data. A driver code is written to control FE and MD processing, as well as information passing.

3.1 Setting up the Relaxed Initial Configuration in Ω_A

Prior to the domain partitioning, the atomistic model is initially created for the entire domain, i.e., $\Omega_T = \Omega_C \bigcup \Omega_A$. For atomistic simulations, the system is set up by placing atoms conforming to the crystallographic lattice configuration. This is followed by energy minimization process under zero-temperature molecular statics conditions to obtain the equilibrium configuration. After the equilibration process, the atoms in the continuum domain $\Omega_C \backslash \Omega_I$ are removed and the finite element mesh is created in Ω_C. In interface region Ω_I, where both atoms and finite element mesh co-exist, the atoms-nodes connection is built by Voronoi tessellation. For domains containing micro-cracks, the interactions between atoms on two sides of the cracks are turned off.

3.2 Sequence of Steps in a Time Step

In a time increment from t to $t + \Delta t$ in the quasi-static analysis, let $\Delta \boldsymbol{U}^C$ and $\Delta \bar{\boldsymbol{U}}^A$ be the converged incremental displacement solutions of the FE nodes in Ω_C and time-averaged atomic motion in Ω_A respectively, i.e.,

$$\begin{aligned} \boldsymbol{U}^C(t+\Delta t) &= \boldsymbol{U}^C(t) + \Delta \boldsymbol{U}^C(t) \ \in \ \Omega_C \quad \text{and} \\ \bar{\boldsymbol{U}}^A(t+\Delta t) &= \bar{\boldsymbol{U}}^A(t) + \Delta \bar{\boldsymbol{U}}^A(t) \ \in \ \Omega_A \end{aligned} \tag{12}$$

The displacement increment $\Delta \boldsymbol{U}^C(t)$ can be further partitioned into a group of displacement increments $\Delta \boldsymbol{U}^{C_I}(t)$ of the interface nodes in $\Omega_{C_I} (\in \Omega_I) = \Omega_C \cap \Omega_A$ and displacement increments $\Delta \boldsymbol{U}^{C_O}(t)$ of all other nodes in $\Omega_{C_O} = \Omega_C \setminus \Omega_I$, i.e.,

$$\Delta \boldsymbol{U}^C(t) = \begin{Bmatrix} \Delta \boldsymbol{U}^{C_I}(t) \\ \Delta \boldsymbol{U}^{C_O}(t) \end{Bmatrix} \tag{13}$$

In the incremental solution process between t and $t + \Delta t$ with equilibrium at the discrete temporal points steps, an incremented external load is typically applied on the external boundary of the coupled system $\partial\Omega_C$. The corresponding discretized equilibrium equations for the continuum system at time $t + \Delta t$ is expressed using Eq. (8a) as

$$\begin{Bmatrix} \boldsymbol{f}_{\text{int}}^{C_I}(t+\Delta t) \\ \boldsymbol{f}_{\text{int}}^{C_O}(t+\Delta t) \end{Bmatrix} - \begin{Bmatrix} \boldsymbol{f}_{\text{ext}}^{C_I}(t+\Delta t) \\ \boldsymbol{f}_{\text{ext}}^{C_O}(t+\Delta t) \end{Bmatrix} + \begin{Bmatrix} \boldsymbol{\lambda}(t+\Delta t) \\ 0 \end{Bmatrix} = 0 \tag{14}$$

where $\boldsymbol{f}_{\text{int}}^{C_I}$ and $\boldsymbol{f}_{\text{int}}^{C_O}$ are the internal nodal force vectors from the strain energy contributions in Ω_{C_O} and Ω_{C_I}, $\boldsymbol{f}_{\text{ext}}^{C_I}$ and $\boldsymbol{f}_{\text{ext}}^{C_O}$ are externally applied load vectors on $\partial\Omega_{C_O}$ and $\partial\Omega_{C_I}$, and $\boldsymbol{\lambda}$ corresponds to the vector of Lagrange multipliers that are associated with displacement constraints in the continuum–atomistic hand-shake region, all at the end of the time step at $(t + \Delta t)$. In an incremental formulation, the vectors are additively decomposed as

$$\begin{aligned} \{\boldsymbol{f}_{\text{int}}^{C}(t+\Delta t)\} &= \{\boldsymbol{f}_{\text{int}}^{C}(t)\} + \{\Delta \boldsymbol{f}_{\text{int}}^{C}\} \\ \{\boldsymbol{f}_{\text{ext}}^{C}(t+\Delta t)\} &= \{\boldsymbol{f}_{\text{ext}}^{C}(t)\} + \{\Delta \boldsymbol{f}_{\text{ext}}^{C}\} \\ \{\boldsymbol{\lambda}(t+\Delta t)\} &= \{\boldsymbol{\lambda}(t)\} + \{\Delta \boldsymbol{\lambda}\} \end{aligned} \tag{15}$$

In every successive iteration step k of the staggered scheme, the internal nodal forces $\{\Delta \boldsymbol{f}_{\text{int}}^{C}\}$ can be expressed in terms of the infinitesimal displacement vector $\{\Delta \boldsymbol{U}^{C}\}$, by neglecting higher order terms, as

$$\{\Delta \boldsymbol{f}_{\text{int}}^{C}\}^{k} = \{\frac{\partial \Delta \boldsymbol{f}_{\text{int}}^{C}}{\partial \Delta \boldsymbol{U}^{C}}\}^{k} \cdot \{\Delta \boldsymbol{U}^{C}\}^{k} = [\boldsymbol{K}^{C}]^{k}\{\Delta \boldsymbol{U}^{C}\}^{k} \tag{16}$$

where $[\boldsymbol{K}^{C}]^{k}$ is the secant stiffness matrix in the kth iteration given as

$$[\boldsymbol{K}^{C}]^{k} = \begin{bmatrix} \boldsymbol{K}^{C-II} & \boldsymbol{K}^{C-IO} \\ \boldsymbol{K}^{C-OI} & \boldsymbol{K}^{C-OO} \end{bmatrix}^{k} = \begin{bmatrix} \boldsymbol{f}_{\text{int}}^{C_I}/(\Delta \boldsymbol{U}^{C_I}) & \boldsymbol{f}_{\text{int}}^{C_I}/(\Delta \boldsymbol{U}^{C_O}) \\ \boldsymbol{f}_{\text{int}}^{C_O}/(\Delta \boldsymbol{U}^{C_I}) & \boldsymbol{f}_{\text{int}}^{C_O}/(\Delta \boldsymbol{U}^{C_O}) \end{bmatrix}^{k} \tag{17}$$

With equilibrium condition satisfied at time t, and the assumption that no external load is not applied on the interface boundary $\partial\Omega_{C_I}$, the Eq. (14) can be rewritten for the kth iteration step as

$$\begin{bmatrix} \boldsymbol{K}^{C-II} & \boldsymbol{K}^{C-IO} \\ \boldsymbol{K}^{C-OI} & \boldsymbol{K}^{C-OO} \end{bmatrix}^{k} \begin{Bmatrix} \Delta \boldsymbol{U}^{C_I} \\ \Delta \boldsymbol{U}^{C_O} \end{Bmatrix}^{k} - \begin{Bmatrix} 0 \\ \Delta \boldsymbol{f}_{\text{ext}}^{C_O} \end{Bmatrix} + \begin{Bmatrix} \Delta \boldsymbol{\lambda} \\ 0 \end{Bmatrix}^{k} = 0 \tag{18}$$

In the staggered-iterative solution approach with successive iteration, displacement error for all nodes in the interface is checked for convergence in iteration step. In the kth iteration, the displacement error tolerance criterion is expressed as

$$\left|\{\Delta \boldsymbol{U}^{C_I} - \Delta \boldsymbol{U}^{A_I}\}^{k}\right|_{max} \leq \epsilon_u \tag{19}$$

where $|\cdot|_{max}$ is the maximum norm and the error tolerance ϵ_u is taken as 0.1 Å. $\Delta \boldsymbol{U}^{A_I}$ is the time-averaged displacement vector at an interface node calculated from the displacement of atoms $\Delta \boldsymbol{U}^{A}$ using Eq. (7), i.e., for each interface node β:

$$\{\Delta \boldsymbol{U}_{\beta}^{A_I}\} = \sum_{p \in G_{\beta}} w_p \cdot \Delta\{\bar{\boldsymbol{U}}_{p}^{A}\} \tag{20}$$

In the time increment from t to $t + \Delta t$, with displacement fields $\Delta \boldsymbol{U}^{C}(t)$ and $\Delta \bar{\boldsymbol{U}}^{A}(t)$ known for iteration step $k \geq 1$, the search for solution fields in the $k + 1$th iteration step proceeds in the following steps.

1. *Displacement increments in* Ω_C: This steps solves the finite element Eqs. (18) for the continuum domain Ω_C with known boundary conditions on the external boundary $\partial\Omega_C^{\text{ext}}$, as well as displacements on the interface nodes in the handshake region Ω_I. The incremental load (or displacement) on $\partial\Omega_C^{\text{ext}}$ is held fixed for the time increment Δt. Updated nodal displacements in the handshake domain Ω_{C_I} are applied in every iteration step corresponding to the atomic displacements in Ω_{A_I} in the previous iteration as

$$\{\Delta \boldsymbol{U}^{C_I}\}^{k+1} = \{\Delta \boldsymbol{U}^{A_I}\}^{k} \tag{21}$$

   Eq. (18) is solved for the displacements $\{\Delta \boldsymbol{U}^{C_O}\}^{k+1}$ and Lagrange multipliers $\{\Delta \boldsymbol{\lambda}\}^{k+1}$ using a nonlinear solver like the Newton–Raphson method or the quasi-Newton method.

2. *Constraint forces on* Ω_{A_I} *from* Ω_{C_I}: With the known vector of Lagrangian multipliers $\{\boldsymbol{\lambda}\}^{k+1} = \{\boldsymbol{\lambda}\}^{k} + \{\boldsymbol{\Delta\lambda}\}^{k+1}$ for all interface nodes, constraint forces on atoms in Ω_{A_I} are evaluated using Eq. (9) as

$$\{\boldsymbol{f}_{p}^{\text{constraint}}\}^{k+1} = \begin{cases} w_p\{\boldsymbol{\lambda}_{\beta}\}^{k+1} & \forall p \in G_{\beta} \in \Omega_{A_I} \\ 0 & \forall p \in \Omega_A \backslash \Omega_{A_I} \end{cases} \tag{22}$$

3. *MD simulations of domain* Ω_A *with constraint forces*: The constraint forces in step II are applied to the atomistic domain Ω_A for MD simulations over a time period of the $T_A = N\Delta t^{md}$ using the velocity Verlet time algorithm (Plimpton, 1995) for integrating Eq. (10). According to Eq. (4), the time-averaged displacement vectors $\{\bar{\boldsymbol{u}}_p\}^{k+1}$ are evaluated as

$$\{\bar{\boldsymbol{u}}_p\}^{k+1} = \frac{1}{N}\sum_{j=0}^{N-1} \boldsymbol{u}_p(t - j \cdot \Delta t^{md}) \;\; \forall p \in \Omega_A \tag{23}$$

4. *Transfer displacements from* Ω_A *to* Ω_C: With the atomic displacements obtained from Eq. (23), $\Delta \boldsymbol{U}_{k+1}^{A_I}$ is calculated using Eq. (20). This serves as the displacement boundary condition for the finite element interface nodes in the next iteration.

3.3 Reducing Stress Fluctuations in the Iterative Process through Sub-Stepping

A draw back of the staggered, successive iterative solution procedure, with a fixed applied load in each increment, is the likelihood of relatively large deviation from the equilibrium configuration in the initial iteration cycles. This effect is demonstrated for an example in Section 3.4 with 40 iterations per loading increment. This corresponds to an upper bound of the total number of iterations k_{tot} within each time step Δt. The average stress in the atomistic region is plotted with the solid line in Fig. 2. The finite stress jumps are attributed to the stress imbalance. To overcome this drawback, a sub-stepping algorithm is implemented, where the load increment is uniformly distributed over a pre-assessed number of sub-steps in the increment. Each continuum–atomistic iteration is conducted over a sub-step $\Delta_k T_A$ of the total time increment $\Delta t = \sum_k^{k_{tot}} \Delta_k T_A$. $\Delta_k T_A$ incorporates N times steps in the MD simulations, i.e., $N = (\Delta_k T_A)/(\Delta t^{md})$. In this work, k_{tot} is taken as 40 and $\Delta_k T_A$ is taken as 1 ps. This corresponds to $\Delta t = 40$ ps. The sub-stepping algorithm results in the same final stress state as shown with the dashed line in Fig. 2, but with stress fluctuations removed. The original scheme is appropriate for finding equilibrium configuration under static load, the sub-stepping scheme is appropriate for investigating critical events under constant strain rate.

A flow chart of the update process in a time step Δt for original scheme is given in Fig. 3. Upon convergence by the criterion (19), the following relations are also satisfied, *viz.*, $\{\Delta \boldsymbol{U}^C\}^{k+1} = \{\Delta \boldsymbol{U}^C\}^k$ and $\{\Delta \bar{\boldsymbol{U}}^A\}^{k+1} = \{\Delta \bar{\boldsymbol{U}}^A\}^k$.

3.4 Convergence Rate of the Iterative Solution Process

The convergence rate, indicated by the number of iteration steps needed for the algorithm (given in Section 3.2 and in Fig. 3) to converge, is investigated in this section. A benchmark test is set up to examine the error due to coupling in the analysis domain. The sample geometry used in this test is shown in Fig. 4, but without the center crack. The material properties are also given in Section 5. A bi-axial tensile displacement is applied on the domain surface in the x and y directions, i.e.,

$$u^1\big|_{x=\pm L} = \pm u_0, \quad u^2\big|_{y=\pm L} = \pm u_0 \tag{24}$$

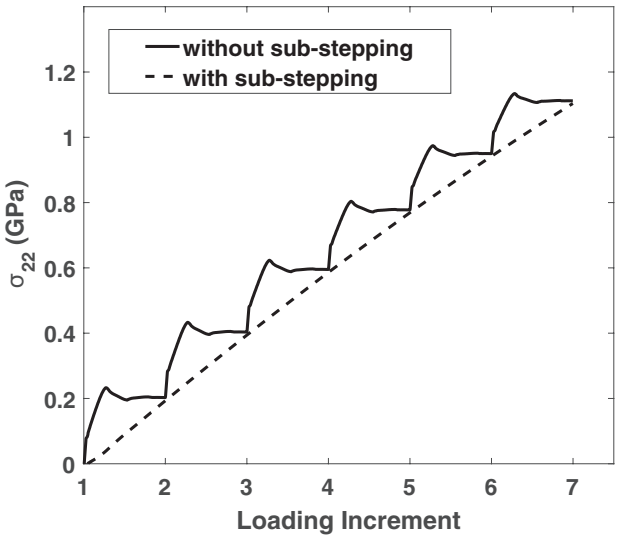

FIG. 2: Average stress in the atomistic region with and without load smoothing

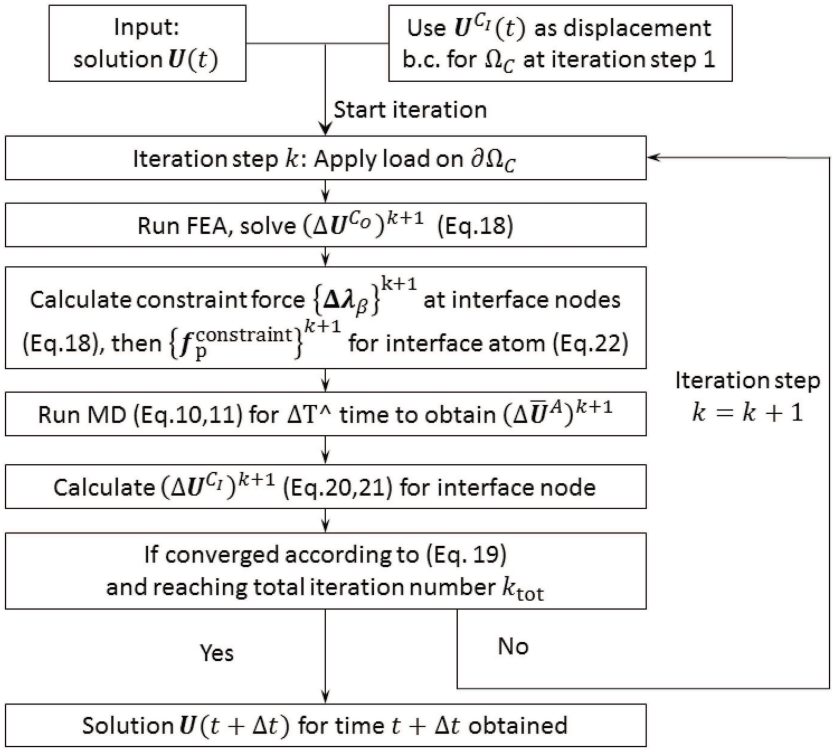

FIG. 3: Flow chart of the iterative solution algorithm for the concurrently coupled model under finite temperature conditions

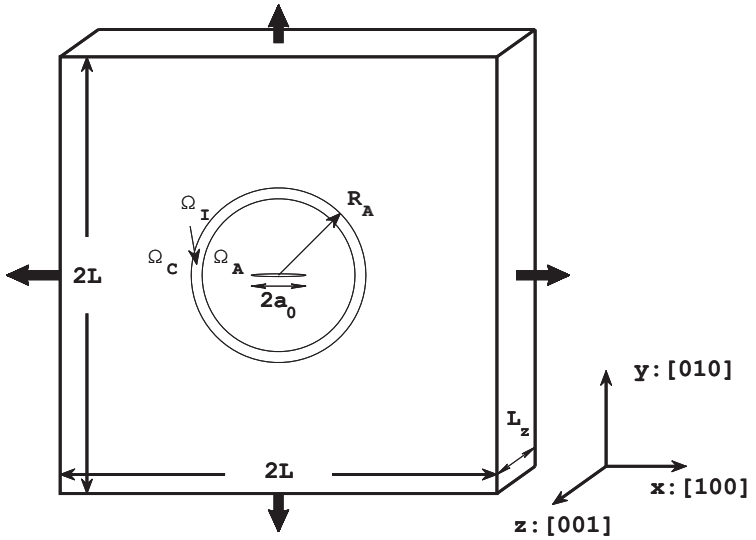

FIG. 4: Geometry of the specimen with loading that is used for crack tip fields study

Periodic boundary condition is applied in the z direction. Ghost-force correction is implemented in the interface domain Ω_I. For a material with homogeneous properties, the analytical displacement solution for a point at location (x,y,z) is given as

$$(u^1)_{\mathrm{anal}} = u_0 \frac{x}{L}$$

Normalized average displacement errors $E_{u^1}^{C/A}$ are, respectively, defined in terms of the square of the difference between the computed and analytical solutions in Ω_C and Ω_A, respectively, as

$$E_{u^1}^{C} = \frac{1}{n_{\text{node}}} \sum_{\alpha=1}^{n_{\text{node}}} \left(\frac{u_\alpha^1 - (u_\alpha^1)_{\text{analy}}}{u_0} \right)^2 \text{ and } E_{u^1}^{A} = \frac{1}{n_{\text{atom}}} \sum_{p=1}^{n_{\text{atom}}} \left(\frac{u_p^1 - (u_p^1)_{\text{analy}}}{u_0} \right)^2 \tag{25}$$

where $u_\alpha^1,\ u_p^1$ are x direction displacement components computed by the coupled concurrent model for a node α and atom p. $(u_\alpha^1)_{\text{analy}}$, $(u_p^1)_{\text{analy}}$ are the corresponding analytical solutions. The average displacement error with and without the sub-stepping algorithm in both Ω_C and Ω_A are plotted with respect to the iteration number in Fig. 5. Without sub-stepping the method uses k successive iteration cycles for convergence. The displacement error is quite large ($>$20%) at early stages of iteration but converges rapidly to very small error values ($<$2%) in 10 to 20 iteration cycles. In contrast, the displacement error with sub-stepping is consistently low at nearly $\sim$2.5% for all the steps in the time interval. Though the displacement error with the sub-stepping algorithm is slightly higher than that without sub-stepping, stress fluctuations with the latter are removed due to the absence of the large error in the first several iterations. This improves the overall accuracy of the coupled concurrent model.

3.5 Ghost-Force Correction

Ghost forces refer to non-physical forces that arise in atomistic–continuum coupling (Tadmor, 1996). These are observed in most energy-based methods and some force-based methods. Methods of alleviating ghost forces have been proposed in (Badia et al., 2008; Curtin and Miller, 2003; Shenoy et al., 1999; Weinan et al., 2006). In the present paper, ghost forces occur at the boundary of the atomistic model Ω_A as a consequence of replacing atoms by continuum material in the interface, thus causing an imbalance of surface atoms with their original neighbors. The difference in the calculated forces on surface atoms before and after replacing atoms with the continuum mesh in the relaxed initial configuration, represents the ghost force. This is expressed as

$$\boldsymbol{f}_p^{\text{g}} = \tilde{\boldsymbol{f}}_p - \boldsymbol{f}_p \quad \forall p \in \Omega_A \tag{26}$$

where $\boldsymbol{f}_p$ is the force on atom p with full atomistic representation and $\tilde{\boldsymbol{f}}_p$ is the force after replacing certain atoms with a continuum mesh. Since the initial configuration is at a minimized energy state and atoms in Ω_A are far from

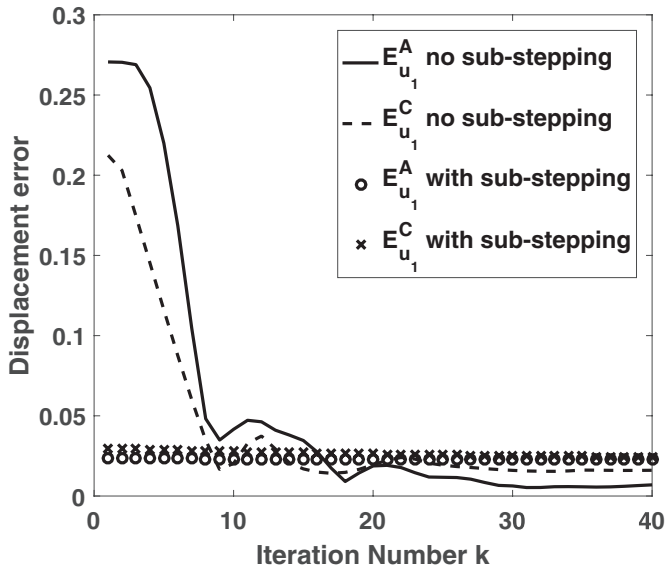

FIG. 5: Displacement error profile with iteration steps with and without sub-stepping

boundaries, $\boldsymbol{f}_p = 0$ and $\boldsymbol{f}_p^{\mathrm{g}} = \tilde{\boldsymbol{f}}_p$. A correction force $\boldsymbol{f}_p^{\mathrm{c}}$ is thus imposed on atom p as an additional external force to annul ghost forces, given as

$$\boldsymbol{f}_p^{\mathrm{c}} = -\boldsymbol{f}_p^{\mathrm{g}} \quad \forall p \in \Omega_A \tag{27}$$

Studies have shown that while deformation dependent ghost forces may not be completely annihilated for any applied loading, the above procedure generally reduces it to acceptable tolerances. To show the effect of ghost-force correction, the relative displacement error in the atomistic region of the coupled model is shown in Fig. 6, both with and without ghost-force correction. The sample and loading conditions, as well as the definition of the relative displacement error is the same as in Section 3.4. The results show that the ghost-force correction reduces the relative displacement error from about 5% to less than 2%.

4. SELF-CONSISTENT HOMOGENIZED CONSTITUTIVE MODELING USING THE COUPLED CONCURRENT MODEL

The self-consistent method proposed in Budiansky (1965) and Hill (1965), estimates the overall material response by embedding a heterogeneous domain in a large homogeneous material with yet unknown macroscopic properties. Self-consistent homogenization evaluates constitutive relations while equilibrating disparate domains under the constraint of kinematic compatibility. This section discusses the development of a self-consistent constitutive model for an elastic crystalline material containing a crack, by using the coupled concurrent computational model. Self-consistency of the governing equations, requires the stress–strain relations in the continuum media to be consistent with the inter-atomic potential of the discrete atomic domain that exclusively contains the crack. The self-consistent model accounts for non-linearity as well as non-locality of the constitutive relations due the existence of material defect or inhomogeneity. The latter is difficult to achieve with most other conventional models like the quasi-continuum models. While the results presented in this section are for single-crystal nickel represented by the EAM potential (Mishin et al., 1999), the approach here is general and can be applied to different materials of interest.

Non-linearity is expected in the material constitutive relation even in the elastic range, due to the non-harmonic atomic interaction described by the EAM potential. Nonlocal constitutive relations are generally associated with size effects and length scales, that may be related to the material microstructure, defects structure, cracks, or features like atomic interaction.

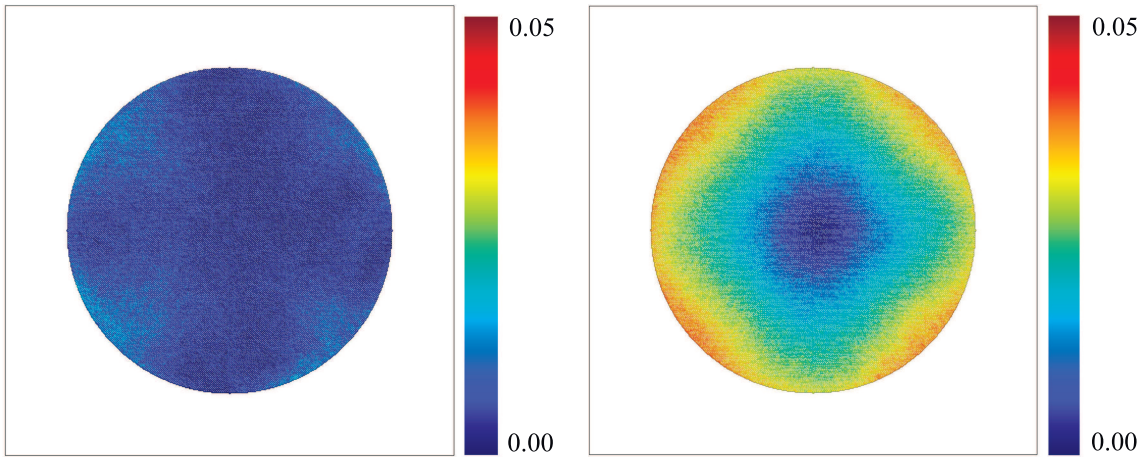

FIG. 6: Distribution of relative displacement error in the atomistic region: (a) with ghost-force correction, (b) without ghost-force correction

In the non-local, non-linear elasticity stress–strain relation, the Cauchy stress can be additively decomposed into two parts as

$$\sigma_{ij} = \sigma_{ij}^{loc} + \hat{\sigma}_{ij} \tag{28}$$

where σ_{ij}^{loc} is the local stress term that is a non-linear function of the strain, and $\hat{\sigma}_{ij}$ is the nonlocal term that is assumed to be a function of the strain gradient in this work. These components are developed next.

4.1 Non-Linear Elastic Constitutive Relation and Parameter Calibration

The non-linear elasticity model is developed with small strain assumptions from a strain energy density function ω that is expressed as a third-order expansion of the infinitesimal strain tensor $\boldsymbol{\epsilon}$ as

$$\omega(\boldsymbol{\epsilon}) = \frac{1}{2!} c_{ijkl}\epsilon_{ij}\epsilon_{kl} + \frac{1}{3!} c_{ijklmn}\epsilon_{ij}\epsilon_{kl}\epsilon_{mn} \tag{29}$$

The local component of the Cauchy stress in Eq. (28) is given as the derivative of the strain energy density with respect to strain as

$$\sigma_{ij}^{loc} = \frac{\partial \omega}{\partial \epsilon_{ij}} = c_{ijkl}\epsilon_{kl} + \frac{1}{2} c_{ijklmn}\epsilon_{kl}\epsilon_{mn} \tag{30}$$

Here c_{ijkl} and c_{ijklmn} correspond to the first- and second-order stiffness coefficients, respectively. For cubic pure nickel single crystals, the coefficients are subjected to crystal symmetry group constraints. Using contracted notations in the representation of the tensors, i.e.,

$$11 \mapsto 1, \quad 22 \mapsto 2, \quad 33 \mapsto 3, \quad 23 \mapsto 4, \quad 31 \mapsto 5, \quad 12 \mapsto 6$$

the coefficients in Eq. (29) are reduced to only three independent coefficients c_{11}, c_{12}, c_{44} for the first-order stiffness and six independent coefficients c_{111}, c_{112}, c_{123}, c_{144}, c_{166}, c_{456} for the second-order stiffness. With $e_4 = e_{23} + e_{32}$, Eq. (30) becomes

$$\begin{aligned} \sigma_1 &= c_{11}e_1 + c_{12}(e_2 + e_3) + c_{123}e_2e_3 + \frac{1}{4}c_{144}e_4^2 + \frac{1}{4}c_{166}(e_5^2 + e_6^2) \\ \sigma_4 &= c_{44}e_4 + 2c_{456}e_5e_6 + c_{144}e_1e_4 + c_{166}e_4(e_2 + e_3) \end{aligned} \tag{31}$$

The first three terms correspond to the harmonic part of the EAM potential and the remaining to the non-harmonic part.

Simulations of the specimen in Fig. 4, without the center crack, by the coupled concurrent model are used to obtain the coefficients in Eq. (31). The specimen is subjected to an increasing bi-axial displacement controlled loading, leading to a strain state up to $\epsilon_{11} = \epsilon_{22} = 4.5\%$. The averaged deformation gradients are evaluated for both the MD and continuum models in the interface Ω_I, denoted as $\boldsymbol{F}^{A_I}$ and $\boldsymbol{F}^{C_I}$, respectively. $\boldsymbol{F}^{C_I}$ is calculated as the volume average over all elements in Ω_{C_I}, while $\boldsymbol{F}^{A_I}$ is the average of deformation gradient for all atoms in Ω_{A_I}. For the small strains in the continuum, the deformation gradient may be expressed in terms of the strain tensor as $\boldsymbol{F} = \boldsymbol{I} + \boldsymbol{\epsilon}$, where $\boldsymbol{I}$ is the identity tensor. The deformation gradient in atomic lattices has been defined in Zimmerman et al. (2009) and implemented in Zhang and Ghosh (2013) using a least-square minimization-based methodology. For a given atomic location $\boldsymbol{x}^p$ and its n nearest neighbors in the deformed atomic configuration, a least-square regression analysis solves for a local-averaged deformation gradient tensor $\boldsymbol{F}^p$ by minimizing each component i of a residual vector B_i^p, defined as

$$B_i^p = \sum_{q=1}^{n} (x_i^{pq} - F_{iJ}^p X_J^{pq})^2 \tag{32}$$

where x^{pq} is an inter-atomic separation vector in the deformed configuration for the p-q near-neighbor pair, and X^{pq} is the corresponding vector in the reference configuration, for each atom p. Components of $\boldsymbol{F}$ in the regression equation are obtained by minimizing B_i^p, i.e., by enforcing the relation

$$\partial B_i^p / \partial F_{iM}^p = 0 \; \forall \; i, M \tag{33}$$

For a material model that is consistent with the atomistic model, compatibility requirements between atomistic and continuum domains necessitate $\boldsymbol{F}^{A_I}$ and $\boldsymbol{F}^{C_I}$ at the interface Ω_I. The calibration of the nine stiffness coefficients in Eq. (31) are based on the minimization of the L_2 norm $\|\boldsymbol{F}^{A_I} - \boldsymbol{F}^{C_I}\|$ in the interface region. Calibrated values of the stiffness coefficients are given in Table 1 and compared with values from experiments and ab-initio calculations in Sarma and Reddy (1973) and Mishin et al. (1999).

The calibrated parameters from the coupled concurrent model simulations generally agree with the values given in the references. Deformation gradient components in the atomistic and continuum portions of the interface Ω_I, i.e., $F_{11}^{A_I}, F_{11}^{C_I}$ and $F_{33}^{A_I}, F_{33}^{C_I}$, are plotted as functions of the applied displacements in Figs. 7(a) and 7(b) with linear and non-linear elasticity assumptions, respectively. The non-linear elasticity stiffness parameters are from Table 1 with the higher order coefficients to zero for linear elastic simulation. Figure 7(a) shows considerable deviation between the continuum and atomistic results, especially at higher levels of deformation. In contrast, for the non-linear elasticity model, the continuum and atomistic deformation gradient components match even at large deformations. The nonlinear elastic model with quadratic dependence on strains is necessary for consistency with the atomistic model.

4.2 Nonlocal Extension of the Nonlinear Elastic Model

The non-local effect is accounted for through the incorporation of gradient elasticity terms in the constitutive relations. The nonlocal component of the Cauchy stress in Eq. (28) may be expressed in terms of the gradients of strain as

$$\hat{\sigma}_{ij} = d_{ijklm}\epsilon_{ij,m} + f_{ijklmn}\epsilon_{ij,mn} \tag{34}$$

where d_{ijklm} and f_{ijklmn} are, respectively, the coefficients associated with the first and second gradients of the strain. Studies in Askes and Aifantis (2011), Aifantis (1984), and Maranganti and Sharma (2007) suggest that the

TABLE 1: Calibrated values of first and second order stiffness coefficients (unit: GPa) and comparison with results in Sarma and Reddy (1973) and Mishin et al. (1999)

Source	c_{11}	c_{12}	c_{44}	c_{111}	c_{112}	c_{123}	c_{144}	c_{166}	c_{456}
Calibrated	244.6	150.8	125.1	–1660	–1220	–250	–130	–510	–65
Ref. Sarma and Reddy (1973)	251.6	154.4	122.0	–2032	–1043	–220	–138	–910	–70
Ref. Mishin et al. (1999)	247	148	125	—	—	—	—	—	—

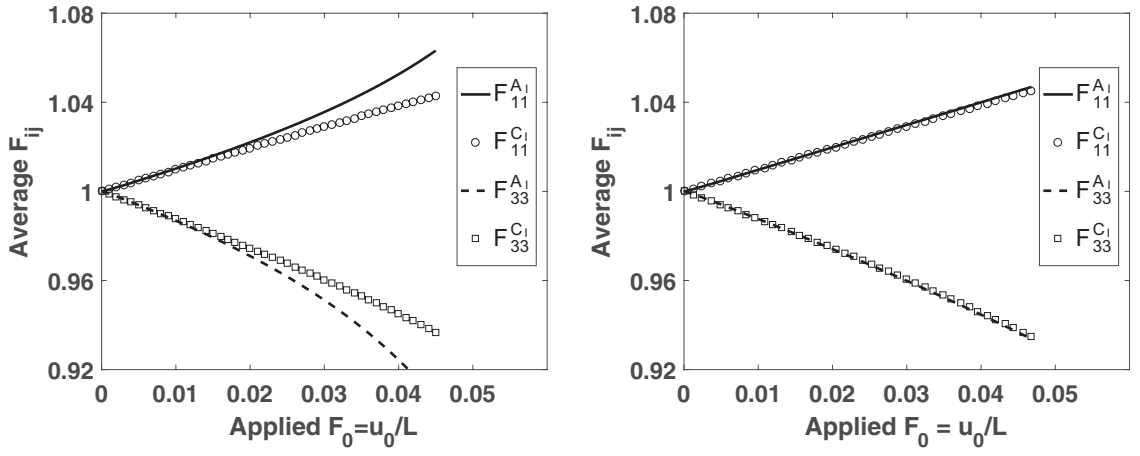

(a) (b)

FIG. 7: Comparison of the averaged deformation gradient in Ω_I by MD and FE simulations with (a) linear and (b) nonlinear elasticity assumptions

first gradient is commonly neglected in the non-local stress representation. For cubic systems, two characteristic length scale parameters, which correspond to the longitudinal and transverse modes of the [100] direction, define the non-local behavior, *viz.*, $l_1 = \sqrt{f_{111111}/c_{1111}}$ and $l_2 = \sqrt{f_{12212}/c_{1212}}$. MD-based studies in Maranganti and Sharma (2007) have evaluated them for copper as $l_1 = l_2 = 0.5$ Å, while for aluminum as $l_1 = 0.9$ Å and $l_2 = 0.9$ Å. In general, continuum models assume a single length-scale parameter l in the non-local stress expression (Aifantis, 1984; Askes and Aifantis, 2011), written as

$$\hat{\sigma}_{ij} = l^2 c_{ijmn} \nabla^2 \epsilon_{mn} \tag{35}$$

where c_{ijmn} are the first-order stiffness coefficients given in Eq. (29). The non-local term is the combined effect of an intrinsic material length-scale l and the local strain gradient that is dependent on topology and loading conditions. Assuming that the K field governs the strain in the vicinity of the crack, i.e.,

$$\epsilon_{ij}(r, \theta) = \frac{A_{ij}}{\sqrt{r}} B_{ij}(\theta) \tag{36}$$

where r is distance from the tip and A_{ij} are constants proportional to the stress intensity factor K_I, Eq. (35) yields

$$\nabla^2 \epsilon_{ij} \propto \frac{1}{r^2} \epsilon_{ij} \tag{37}$$

Correspondingly, the ratio $\hat{\sigma}_{ij}/\sigma_{ij}^{\text{loc}} \sim \mathcal{O}(l^2/r^2)$. Thus, if the distance of continuum elements from crack tip is $r \gg l$, nonlocal elasticity may be ignored.

Calibration of the length-scale parameter is done by conducting molecular statics simulation of a single-crystal nickel specimen with a center crack as shown in Fig. 8(a) that is introduced to create a strain-gradient field. The specimen dimensions are $L_x = L_y = 50$ nm, $L_z = 4.224$ nm, and the crack is of length $2a_0 = 20$ nm in the xz plane through the z direction. A biaxial displacement loading is applied in the x and y directions on the lateral boundaries, while periodic boundary condition with stress-free conditions are applied on the z-faces. To evaluate the non-local stresses $\hat{\sigma}_{ij}$, the virial stress field σ_{ij} and the local stress field σ_{ij}^{loc} are calculated using Eq. (30) and parameters in Table 1. This is followed by evaluating the local deformation gradient and strain fields using Eq. (32). Figure 8(b) plots the stress $\hat{\sigma}_{22} = \sigma_{ij} - \sigma_{ij}^{\text{loc}}$ as a function of $[-c_{22mn}\nabla^2\epsilon_{mn}]$ for atoms in the x direction in front of crack tip. The calibrated length-scale parameter l^2 for nickel using the EAM potential, corresponding to the slope of this plot is $l \approx 0.5$ Å. This is consistent with values for copper and aluminum.

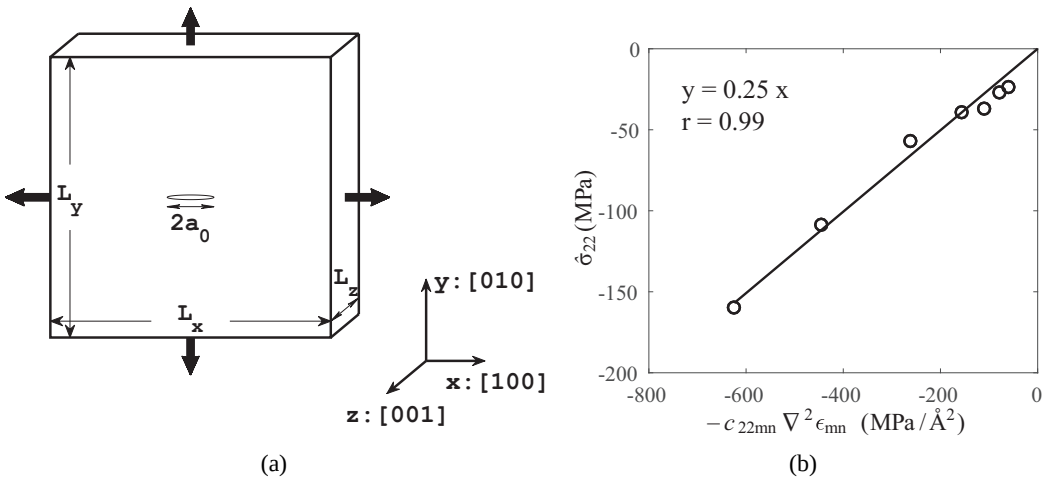

(a) (b)

FIG. 8: (a) Nickel specimen with EAM potential for molecular statics simulation on sample with an embedded center crack, and (b) plot of the nonlocal stress as a function of strain gradient. The slope corresponds to the square of l^2

In this paper, the crack tip is kept from entering the interface region for numerical stability purposes. With a typical choice of $\sim$5 nm for the interface width, the distance from any continuum element to the crack tip is larger than $\sim$5 nm. For these dimensions, the ratio $l^2/r^2 \approx 10^{-4} \ll 1$, which suggests that the non-local effect for the continuum domain in the coupled concurrent model in metallic system is very small. However, as given in Maranganti and Sharma (2007), for materials such as polymers where long-range forces exist, the nonlocal effect could be several orders of magnitude higher and should not be neglected.

5. CRACK TIP FIELDS IN SINGLE-CRYSTAL NICKEL

The coupled concurrent model is employed to investigate the stress fields in the vicinity of a crack tip that is contained in the atomistic domain Ω_A. Results of the coupled model are compared with those from a purely finite element analysis implementing the continuum non-linear and non-local elastic constitutive relation developed in Section 4. This comparison is used to verify the accuracy of the self-consistent constitutive relation in predicting crack tip fields. The effects of nonlinearity and nonlocality are also explored.

The specimen geometry and loads used for simulations using the coupled concurrent model are shown in Fig. 9(a). The thickness of the domain in the z direction is $L_z = 4.224$ nm. The atomistic domain Ω_A is a cylinder with a radius $R_A = 32$ nm. The dimensions of the entire coupled model including continuum and atomistic domains 200 nm × 200 nm in the x-y plane. The atomistic domain Ω_A contains about 1.3 million atoms. If the entire domain Ω_T is modeled as a atomistic domain for a nickel single crystal, it would contain about 15 million atoms with a pure MD model. The interface region Ω_I has a thickness of 4 nm, i.e., it is an annular ring region with inner and outer radius 28 nm and 32 nm, respectively. The atomistic structure of nickel is face centered cubic (f.c.c.) with lattice constant 3.52 Å. The orientation is set as $x \to [100]$, $y \to [010]$, $z \to [001]$. A static crack is created in the center of the xz-plane with length $2a_0 = 20$ nm as shown in Fig. 4. The crack passes through the z direction. The continuum domain is discretized into about $20,000$ four-noded, constant strain tetrahedron elements with 5000 nodes. The finite element model for the pure continuum domain is shown in Fig. 9(b). The specimen dimensions and boundary conditions are the same as for the coupled concurrent model. The entire domain is discretized into about $20,000$ constant strain tetrahedron elements. For this problem, the crack is introduced in the FE model by setting the material stiffness to 0.01% of its original value for elements containing the crack. The coupled concurrent model and the pure FE models are shown in Fig. 9.

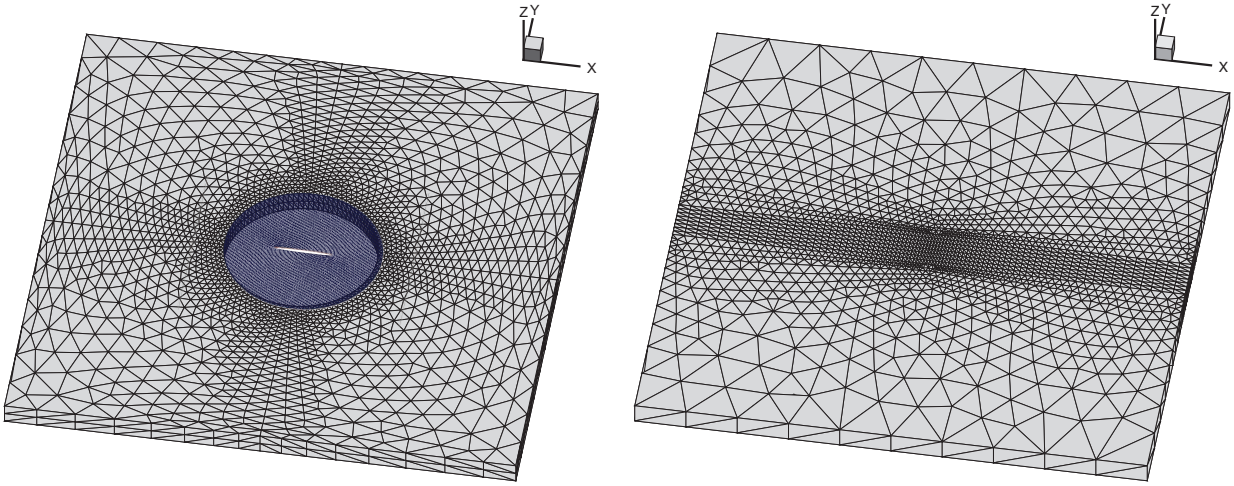

(a) (b)

FIG. 9: (a) FE mesh for the continuum domain and the atomistic domain in the coupled concurrent model with a crack, and (b) the FE mesh in the pure continuum model

In the concurrent model, an initial relaxation process is applied as discussed in Section 3.1. Subsequently, a bi-axial displacement loading is applied on the boundary of continuum domain in the x and y directions. Periodic boundary condition with stress-free boundary conditions are applied in the z direction. The continuum domain uses the non-linear–non-local elasticity relation in Eq. (28) developed in Section 4. It will be shown that the effect of non-local elasticity is negligible in comparison with the non-linearity effects. The temperature of the atomistic domain is set to 1 K using the Langevin thermostat with the NVE ensemble. For the MD simulations, the time step for integration $\Delta t^{md} = 2$ fs, as discussed in Section 3.2. Each sub-step $\Delta_k T_A$ in the continuum–atomistic iteration incorporates $N = 500$ times steps, and hence $\Delta_k T_A = 1$ ps. The applied strain rate is 5×10^8 s^{-1}.

The displacements applied on the x-y boundaries of both models correspond to bi-axial straining of $\epsilon_{11} = \epsilon_{22} = 3\%$. Furthermore, $\sigma_{33} = 0$ on the z faces. The contour plot of the stress σ_{22} in the coupled model is shown in Fig. 10. In Fig. 11(a), the stress σ_{22} ahead of the crack tip along the crack plane by both models is plotted as a function of the distance from the tip. A comparison analytical solution for isotropic linear elasticity is also shown in this figure. The crack-tip analytical stress is given as

$$\sigma_{22} = \sigma_0 \frac{r}{\sqrt{r_1 r_2}} \tag{38}$$

where σ_0 is the far-field stress and r_1, r_2, and r are the distances from the two crack tips and its center, respectively. Figure 11(a) shows good agreement between the coupled concurrent model and the FE model using the constitutive relation of Eq. (28). The FE model using isotropic linear elasticity, as well as the analytical model over-predict the stress value.

Figure 11(b) shows the contributions of the non-linear term [second term in the RHS of Eq. (30)], and the nonlocal term [$\hat{\sigma_{ij}}$ in Eq. (28)], to the stress σ_{22} evaluated by the continuum FE model. The effect of both non-linear and non-local terms decreases with increasing distance from the crack tip. The contribution of the overall non-linear term is more than 10% near the crack tip and about 3% at larger distances. The stress values are over-predicted in the absence of the non-linear term, especially near the crack tip. The contribution of the non-local term is generally orders of magnitude smaller in comparison with the non-linear term. However as the distance from the crack tip r approaches the non-local length scale l, the non-local effect, associated with the second gradient of the strain, increases rapidly and becomes non-negligible.

Finally, a comparison of the cost of computational analysis by the full atomistic MD model, the coupled concurrent model, and the full finite element model with the self-consistent constitutive relations is given in Table 2. The

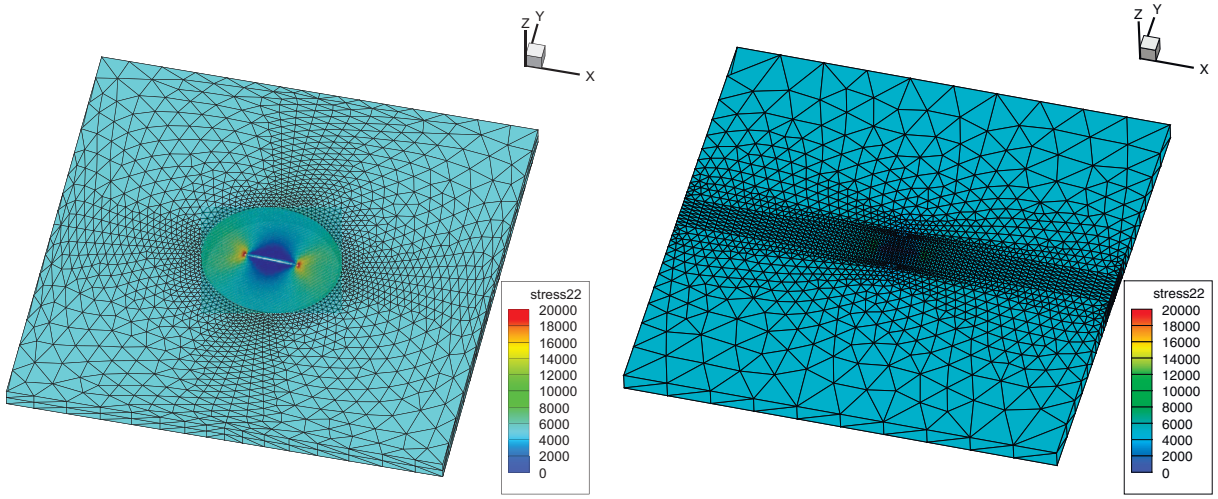

(a) (b)

FIG. 10: Contour plot of the Cauchy stress σ_{22} for (a) the coupled concurrent model, (b) pure FE model with non-linear and non-local elasticity

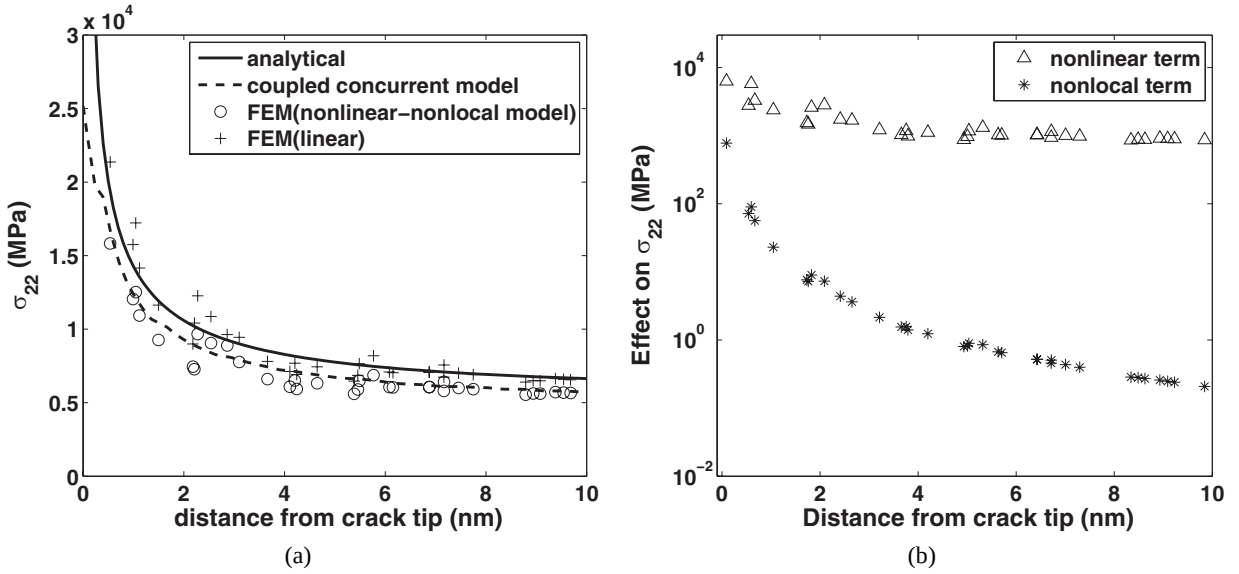

FIG. 11: (a) Stress σ_{22} ahead of the crack tip along the crack plane by different models as a function of the distance from the tip; (b) contributions from the nonlinear and nonlocal terms to the stress σ_{22} by the FE model

TABLE 2: Comparison of computational cost of analyzing the specimen using different models in CPU hours

Method	MD	Coupled atomistic–continuum	Continuum FE
DOF	1.6×10^7 atoms	1.6×10^6 atoms + 2×10^4 elements	2×10^4 elements
CPU hours	300	40	0.5

comparison is made for a specimen with dimensions $L_x = L_y = 200$ nm, $L_z = 4.224$ nm with a center crack. The boundary conditions are similar to that discussed before, but going up to strains $\epsilon_{xx} = \epsilon_{yy} = 3\%$. The results show a significant reduction (by a factor of 7.5) in computational cost from full MD to the coupled continuum–atomistic model and another significant reduction (by a factor of 80) when using the full FE model. A speed-up by a factor of 600 is achieved by going from the full MD to full FE simulations. This shows that the proposed self-consistent multi-scale framework is able to efficiently simulate micro-scale experiments, while accurately keeping track of the material behavior with origins at the atomistic length scale.

6. SUMMARY AND DISCUSSION

This paper has developed a methodology for deriving self-consistent, reduced order constitutive relations of elastic crystalline materials containing atomistic scale cracks by using a concurrent atomistic–continuum computational modeling framework. The resulting constitutive model for cracked materials incorporates both non-linearity and nonlocality to account for atomic level interactions and deformation mechanisms especially near crack tips. Atomistic scale simulations are necessary for a physical understanding of the evolution of these mechanisms. As a vehicle for developing the self-consistent model, a concurrent computational framework coupling atomistic and crystalline continuum domains is first accomplished. Atomistic modeling is done using molecular dynamics (MD) using LAMMPS, while the continuum modeling for quasi-static loading is done using a crystal elasticity finite element analysis code. Finite temperature is applied on the atomistic domain using Langevin dynamics for the MD model. The concurrent framework accommodates both physical boundary conditions and atomic resolutions at locations of interest, such as the crack tip. The atomistic–continuum coupling is achieved by enforcing geometric compatibility and force

equilibrium in a finite-thickness handshake or interface region. A staggered-iterative approach is used to solve the coupled system with optimized parallel implementation using LAMMPS and the FE code.

Non-linearity and non-locality characteristics are incorporated in the elastic constitutive relation to ensure self-consistency of the continuum material description with that at the atomistic level the the MD simulations using potential functions and with explicit crack representation in the concurrent framework. Non-linearity is accounted for through higher-order strain terms, while non-locality is incorporated in the form of strain gradients. The model is calibrated by comparing with results of MD predictions in the concurrent model. For validating the constitutive relation, the crack tip stress field is investigated using both the coupled concurrent model and a finite element model with the non-linear and non-local elastic constitutive law. The effect of non-linearity and non-locality on the crack tip stresses are investigated. The self-consistent model shows excellent agreement and accuracy with the results of the concurrent model. Additionally, an analysis of the computational cost of simulation by the full MD, coupled model, and full FE model shows significantly enhanced efficiency with the self-consistent model. Extension of this coupled model to formulate constitutive models for crack propagation and plasticity is currently underway and will be reported in future publications.

ACKNOWLEDGMENTS

This work has been supported by a mechanics of materials and strength, materials and surface engineering research program sponsored by the National Science Foundation, Mechanics and Structure of Materials Program through grant no. CMMI-1200231 (Program Manager: Dr. Alexis Lewis). The authors gratefully acknowledge this support. Computing support by the Homewood High Performance Compute Cluster (HHPC) and Maryland Advanced Research Computing Center (MARCC) is gratefully acknowledged.

REFERENCES

Abraham, F., Brodbeck, D., Rudge, W., and Xu, X., A molecular dynamics investigation of rapid fracture mechanics, *J. Mech. Phys. Solids*, vol. **45**, pp. 1595–1619, 1997.

Aifantis, E.C., On the microstructural origin of certain inelastic models, *J. Eng. Mater. Tech.*, vol. **106**, no. 4, pp. 326–330, 1984.

Askes, H. and Aifantis, E.C., Gradient elasticity in statics and dynamics: An overview of formulations, length scale identification procedures, finite element implementations and new results, *Int. J. Solids Struct.*, vol. **48**, pp. 1962–1990, 2011.

Badia, S., Bochev, P., Lehoucq, R., Parks, M., Fish, J., Nuggehally, M.A., and Gunzburger, M., A force-based blending model foratomistic-to-continuum coupling, *Int. J. Multiscale Comput. Eng.*, vol. **5**, no. 5, pp. 381–406, 2007.

Badia, S., Parks, M., Bochev, P., Gunzburger, M., and Lehoucq, R., On atomistic-to-continuum coupling by blending, *Multiscale Model. Simul.*, vol. **7**, no. 1, pp. 381–406, 2008.

Budiansky, B., On the elastic moduli of some heterogeneous materials, *J. Mech. Phys. Solids*, vol. **13**, pp. 223–227, 1965.

Columbus, D. and Grujicic, M., A comparative discrete-dislocation/nonlocal crystal-plasticity analysis of plane-strain mode I fracture, *Mater. Sci. Eng. A*, vol. **180**, pp. 138–161, 2001.

Curtin, W.A. and Miller, R.E., Atomistic/continuum coupling in computational materials science, *Model. Simul. Mater. Sci. Eng.*, vol. **11**, no. 3, R33, 2003.

Davydov, D., Pelteret, J.P., and Steinmann, P., Comparison of several staggered atomistic-to-continuum concurrent coupling strategies, *Comput. Methods Appl. Mech. Eng.*, vol. **277**, pp. 260–280, 2014.

Dewald, M.P. and Curtin, W.A., Multiscale modelling of dislocation/grain-boundary interactions: I. Edge dislocations impinging on $\Sigma 11$ (113) tilt boundary in Al, *Model. Simul. Mater. Sci. Eng.*, vol. **15**, no. 1, S193, 2007.

Farrissey, L., Ludwig, M., McHugh, P.E., and Schmauder, S., An atomistic study of void growth in single crystalline copper, *Comput. Mater. Sci.*, vol. **18**, no. 1, pp. 102–117, 2000.

Fish, J. and Chen, W., Discrete-to-continuum bridging based on multigrid principles, *Comput. Methods Appl. Mech. Eng.*, vol. **193**, pp. 1693–1711, 2004.

Fish, J., Nuggehally, M.A., Shephard, M.S., Picu, C.R., Badia, S., Parks, M.L., and Gunzburger, M., Thermostatted molecular

dynamics: How to avoid the Toda demon hidden in Nosé-Hoover dynamics, *Comput. Methods Appl. Mech. Eng.*, vol. **196**, pp. 4548–4560, 2007.

Ghosh, S., *Micromechanical Analysis and Multi-Scale Modeling Using the Voronoi Cell Finite Element Method*, Boca Raton, FL: CRC Press/Taylor & Francis, 2011.

Grujicic, M., Cao, G., and Batchu, S., Crystal plasticity-based finite element analysis of deformation and fracture of polycrystalline lamellar γ-tial $+\alpha 2$-Ti_3Al alloys, *J. Mater. Sci.*, vol. **38**, pp. 209–232, 2003.

Gumbsch, P., An atomistic study of brittle fracture: Toward explicit failure criteria from atomistic modeling, *J. Mater. Res.*, vol. **10**, pp. 2897–2907, 1995.

Hill, R., A self-consistent mechanics of composite materials, *J. Mech. Phys. Solids*, vol. **13**, pp. 213–222, 1965.

Holian, B.L., Voter, A.F., and Ravelo, R., Thermostatted molecular dynamics: How to avoid the Toda demon hidden in Nosé-Hoover dynamics, *Phys. Rev. E*, vol. **52**, pp. 2338–2347, 1995. http://link.aps.org/doi/10.1103/PhysRevE.52.2338

Junge, T., Anciaux, G., and Molinari, J.F., Dynamic stability of displacement-based atomistic/continuum coupling methods, *J. Mech. Phys. Solids*, vol. **80**, pp. 103–120, 2015.

Kadau, K., Germann, T., and Lomdahl, P., Molecular dynamics comes of age: 320-billion-atom simulation on BlueGene/L, *Int. J. Mod. Phys.*, vol. **17**, pp. 1755–1761, 2006.

Kohlhoff, S., Gumbsch, P., and Fischmeister, H.F., Crack propagation in b.c.c. crystals studied with a combined finite-element and atomistic model, *Philos. Mag. A*, vol. **64**, pp. 851–878, 1991.

Maranganti, R. and Sharma, P., A novel atomistic approach to determine strain-gradient elasticity constants: Tabulation and comparison for various metals, semiconductors, silica, polymers and the (ir) relevance for nanotechnologies, *J. Mech. Phys. Solids*, vol. **55**, no. 9, pp. 1823–1852, 2007.

Miller, R., Ortiz, M., Phillips, R., Shenoy, V., and Tadmor, E., Quasicontinuum models of fracture and plasticity, *Eng. Fract. Mech.*, vol. **61**, no. 3, pp. 427–444, 1998.

Miller, R.E. and Tadmor, E.B., A unified framework and performance benchmark of fourteen multiscale atomistic/continuum coupling methods, *Model. Simul. Mater. Sci. Eng.*, vol. **17**, no. 5, 053001, 2009.

Mishin, Y., Farkas, D., Mehl, M., and Papaconstantopoulos, D., Interatomic potentials for monoatomic metals from experimental data and ab initio calculations, *Phys. Rev. B*, vol. **59**, no. 5, 3393, 1999.

Ortiz, M. and Pandolfi, A., Temperature and strain-rate dependence of surface dislocation nucleation, *Int. J. Numer. Methods Eng.*, vol. **44**, pp. 1267–1282, 1999.

Pavia, F. and Curtin, W., Parallel algorithm for multiscale atomistic/continuum simulations using lammps, *Model. Simul. Mater. Sci. Eng.*, vol. **23**, no. 5, 055002, 2015.

Picu, R., Atomistic-continuum simulation of nano-indentation in molybdenum, *J. Comput.-Aided Mater. Des.*, vol. **7**, no. 2, pp. 77–87, 2000.

Plimpton, S., Fast parallel algorithms for short-range molecular dynamics, *J. Comput. Phys.*, vol. **117**, pp. 1–19, 1995.

Qu, S., Shastry, V., Curtin, W.A., and Miller, R.E., A finite-temperature dynamic coupled atomistic/discrete dislocation method, *Model. Simul. Mater. Sci. Eng.*, vol. **13**, no. 7, 1101, 2005.

Roe, K.L. and Siegmund, T., An irreversible cohesive zone model for interface fatigue crack simulation, *Int. J. Numer. Methods Eng.*, vol. **70**, pp. 307–322, 2003.

Saether, E., Yamakov, V., and Glaessgen, E.H., An embedded statistical method for coupling molecular dynamics and finite element analyses, *Int. J. Numer. Methods Eng.*, vol. **78**, no. 11, pp. 1292–1319, 2009.

Sarma, V. and Reddy, P., Third-order elastic constants of single crystal nickel at 80 K, *Phys. Stat Solidi (A)*, vol. **16**, no. 2, pp. 413–418, 1973.

Shenoy, V., Miller, R., Tadmor, E., Rodney, D., Phillips, R., and Ortiz, M., An adaptive finite element approach to atomic-scale mechanics: The quasicontinuum method, *J. Mech. Phys. Solids*, vol. **47**, no. 3, pp. 611–642, 1999.

Shimomura, Y., Kiritani, M., and Mukouda, I., Computer simulation study of the atomistic mechanism of deformation and fracture initiation in thin fcc metal films, *Mater. Sci. Eng. A*, vol. **350**, no. 1-2, pp. 238–244, 2003.

Spearot, D., Jacob, K., and McDowell, D., Non-local separation constitutive laws for interfaces and their relation to nanoscale simulations, *Mech. Mater.*, vol. **36**, pp. 825–847, 2004.

Tadmor, E.B., The Quasicontinuum Method, PhD thesis, Brown University, 1996.

Wagner, G.J. and Liu, W.K., Coupling of atomistic and continuum simulations using a bridging scale decomposition, *J. Comput. Phys.*, vol. **190**, no. 1, pp. 249–274, 2003.

Warner, D.H., Curtin, W.A., and Qu, S., Rate dependence of crack-tip processes predicts twinning trends in f.c.c. metals, *Nat. Mater.*, vol. **6**, pp. 876–881, 2007.

Weinan, E., Lu, J., and Yang, J.Z., Uniform accuracy of the quasicontinuum method, *Phys. Rev. B*, vol. **74**, no. 21, 214115, 2006.

Xiao, S. and Belytschko, T., A bridging domain method for coupling continua with molecular dynamics, *Comput. Methods Appl. Mech. Eng.*, vol. **193**, no. 17, pp. 1645–1669, 2004.

Xiong, L., Deng, Q., Tucker, G.J., McDowell, D.L., and Chen, Y., Coarse-grained atomistic simulations of dislocations in Al, Ni and Cu crystals, *Int. J. Plasticity*, vol. **38**, pp. 86–101, 2012.

Xu, T., Stewart, R., Fan, J., Zeng, X., and Yao, A., Bridging crack propagation at the atomistic and mesoscopic scale for BCC-Fe with hybrid multiscale methods, *Eng. Fract. Mech.*, vol. **155**, pp. 166–182, 2016.

Yamakov, V., Saether, E., Phillips, D.R., and Glaessgen, E.H., Molecular-dynamics simulation-based cohesive zone representation of intergranular fracture processes in aluminum, *J. Mech. Phys. Solids*, vol. **54**, no. 9, pp. 1899–1928, 2006.

Yamakov, V., Saether, E., and Glaessgen, E., Multiscale modeling of intergranular fracture in aluminum: Constitutive relation for interface debonding, *J. Mater. Sci.*, vol. **43**, pp. 7488–7494, 2008.

Yamakov, V., Warner, D., Zamora, R., Saether, E., Curtin, W., and Glaessgen, E., Investigation of crack tip dislocation emission in aluminum using multiscale molecular dynamics simulation and continuum modeling, *J. Mech. Phys. Solids*, vol. **65**, pp. 35–53, 2014.

Yang, Q. and To, A.C., Multiresolution molecular mechanics: A unified and consistent framework for general finite element shape functions, *Comput. Methods Appl. Mech. Eng.*, vol. **283**, pp. 384–418, 2015.

Zhang, J. and Ghosh, S., Molecular dynamics based study and characterization of deformation mechanisms near a crack in a crystalline material, *J. Mech. Phys. Solids*, vol. **61**, no. 8, pp. 1670–1690, 2013.

Zhou, S., Lomdahl, P., Voter, A., and Holian, B., A molecular dynamics investigation of rapid fracture mechanics, *Eng. Fract. Mech.*, vol. **61**, pp. 173–187, 1998.

Zhou, X., Zimmerman, J., Reedy, E., and Moody, N., Molecular dynamics simulation based cohesive surface representation of mixed mode fracture, *Mech. Mater.*, vol. **40**, pp. 832–845, 2008.

Zhu, T., Li, J., and Yip, S., Atomistic study of dislocation loop emission from a crack tip, *Phys. Rev. Lett.*, vol. **93**, no. 2, p. 025503, 2004.

Zimmerman, J.A., Bammann, D.J., and Gao, H., Deformation gradients for continuum mechanical analysis of atomistic simulations, *Int. J. Solids Struct.*, vol. **46**, no. 2, pp. 238–253, 2009.